The Journal of Experimental Biology 214, 2283-2291

doi:10.1242/jeb.050716

RESEARCH ARTICLE

Characteristics of vortex formation and thrust performance in drag-based paddling propulsion

Daegyoum Kim and Morteza Gharib*

Division of Engineering and Applied Science, California Institute of Technology, Pasadena, CA 91125, USA

*Author for correspondence (mgharib@caltech.edu)

Accepted 4 April 2011

SUMMARY

Several characteristics of drag-based paddling propulsion are studied with a simple mechanical model and a measurement technique for mapping three-dimensional flow fields. In drag-based propulsion, the temporal change of the vortex strength is an important parameter in the relationship between vortex formation and thrust generation. Our results indicate that spanwise flow behind the paddling propulsor significantly affects tip vortex development and thrust generation. The distribution of spanwise flow is dependent on the propulsor shape and the Reynolds number. A delta-shaped propulsor generates strong spanwise flow compared with a rectangular propulsor. For the low Reynolds number case, spanwise flow is not as strong as that for the high Reynolds number case. Without sacrificing total impulse, the flexible propulsor can smooth out thrust peaks during sudden stroke motions, which is favorable for avoiding structural failures and stabilizing body motion. We also explored the role of stopping vortex shedding in efficient thrust generation by determining the relationship between stroke angles and total impulses generated by paddling propulsors.

Supplementary material available online at http://jeb.biologists.org/cgi/content/full/214/13/2283/DC1

Key words: drag-based propulsion, vortex, thrust, paddling, rowing.

INTRODUCTION

The locomotion mechanism of flapping animals can be categorized into two modes: lift-based and drag-based propulsions (Vogel, 2003). In lift-based propulsion, most propulsive force acts perpendicularly to the moving direction of the flapper, with a small angle of attack. In drag-based propulsion, with a large angle of attack such as in paddling and rowing modes, the propulsive force acts on the flapper mainly in the direction opposite to the moving direction of the flapper. Vogel conjectured that the lift-based propulsion mode was more efficient in high-speed locomotion, establishing why fast-moving flapping animals employed this mode (Vogel, 2003). He also argued that the drag-based mode was effective in low-speed locomotion in that it could generate large thrust over a short time. Therefore, the drag-based propulsion mode is preferred in maneuvering behaviors such as acceleration, turning and braking (Walker and Westneat, 2000).

The traditional fixed-wing aerodynamic theory has been successfully used in the past to explain the principle of lift-based propulsion. However, this approach is not suitable for drag-based propulsion. The blade-element approach has been used to study the thrust and mechanical efficiency of drag-based propulsion, specifically in the pectoral fin motion of the angelfish (Blake, 1979; Blake, 1980) and the threespine stickleback (Walker, 2004). In addition, vortex structures in the wake were identified experimentally and used to derive the hydrodynamic force acting on the fish (Drucker and Lauder, 1999; Epps and Techet, 2007).

The fundamental difference in the thrust-generation mechanism between lift-based and drag-based propulsion can be better understood by examining the vortex formation process. The hydrodynamic (aerodynamic) force (**F**) acting on a moving object inside an infinite flow field can be derived from the vorticity distribution of the flow field and the velocity of the object (Wu, 1981):

$$\mathbf{F}(t_\mathrm{d}) = -\frac{\rho_\mathrm{f}}{2}\frac{\mathrm{d}}{\mathrm{d}t_\mathrm{d}}\int_{V_\infty}\mathbf{x}_\mathrm{d}\times\boldsymbol{\omega}_\mathrm{d}\,\mathrm{d}V + \rho_\mathrm{f}\frac{\mathrm{d}}{\mathrm{d}t_\mathrm{d}}\int_{V_\mathrm{b}}\mathbf{u}_\mathrm{d}\,\mathrm{d}V\ , \qquad (1)$$

where ρ_f is fluid density, V_∞ is an infinite flow field, V_b is body volume, $\mathbf{x}_\mathrm{d}$ is coordinate, $\boldsymbol{\omega}_\mathrm{d}$ is vorticity, $\mathbf{u}_\mathrm{d}$ is velocity and t_d is time. It is assumed that fluid is static at infinity and the flow is caused only by the motion of the object. This equation is applied generally to viscous flow of any Reynolds number (*Re*). If vorticity is confined in a thin closed vortex loop of circulation (Γ_d) and the object is thin, Eqn 1 can simply be approximated as follows (Wu et al., 2006):

$$\mathbf{F}(t_\mathrm{d}) \approx -\rho_\mathrm{f}\frac{\mathrm{d}}{\mathrm{d}t_\mathrm{d}}(\Gamma_\mathrm{d}\mathbf{S}) = -\rho_\mathrm{f}(\dot{\Gamma}_\mathrm{d}\mathbf{S} + \Gamma_\mathrm{d}\dot{\mathbf{S}}), \qquad (2)$$

where **S** is the vector of the minimum surface spanned by the vortex loop and $|\mathbf{S}|$ is the area of the surface. At very low *Re*, vorticity is diffused quickly and is not confined in a thin closed vortex loop. In that case, Eqn 2 will not be applicable. In contrast, at high *Re*, Eqn 2 may be used as a rough estimate for a thin vortex loop. If propulsive force (F_p) is applied to the object in the negative *x*-direction, then:

$$F_\mathrm{p}(t_\mathrm{d}) = -F_x(t_\mathrm{d}) \approx \rho_\mathrm{f}(\dot{\Gamma}_\mathrm{d}S_x + \Gamma_\mathrm{d}\dot{S}_x), \qquad (3)$$

where S_x is the area of **S** projected on the *y*–*z* plane. Eqns 2 and 3 show that the increase in the area enclosed by the vortex loop ($\dot{\mathbf{S}}$ and $\dot{S}_x$) and the growth of circulation ($\dot{\Gamma}_\mathrm{d}$) are correlated with force generation. Fig. 1 illustrates two simple examples of force generation

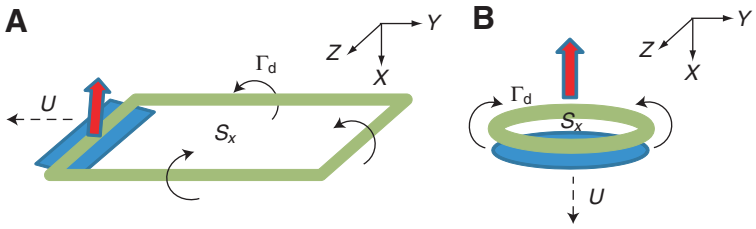

Fig. 1. Vortex structures in (A) lift-based and (B) drag-based propulsion. The thick green line is the vortex generated by a moving object. The curved arrows around the vortex show the rotating direction of the vortex. The dashed arrow indicates the direction of the movement of the object. The thick arrow indicates the direction of force acting on the object.

modes: lift-based and drag-based propulsion. When a flying animal glides with a constant speed and a small angle of attack (Fig. 1A), the circulation of the vortex structure is assumed to be constant in time; the first term ($\dot{\Gamma}_d S_x$) on the right-hand side of Eqn 3 is neglected in lift generation. To apply Eqn 3 to drag-based propulsion, we first consider the example of a falling circular disk whose face is perpendicular to the falling direction (Fig. 1B). Vorticity is assumed to be created at the edge of the disk and the vortex is rolled up around the edge of the disk. In this case, although the inner area of the vortex loop can be assumed to be approximately constant, the circulation growth of the vortex loop cannot be neglected, and the first term ($\dot{\Gamma}_d S_x$) of Eqn 3 contributes significantly to the lift generation of the falling disk. Of course, for drag-based propulsion modes such as paddling and rowing, in which the propulsor rotates with a joint, the vortex structure is not simple. Moreover, the bound vortex, which is a part of the vortex loop, is widely distributed on the surface of the rotating propulsor. In this case, we should also consider the temporal change of a vortex inner area projected in the thrust direction.

In drag-based propulsion, there are several factors that affect thrust performance. The shape of a propulsor and its deformation are important factors in evaluating thrust performance. For example, the optimal shape of a rowing appendage is a distally expanding shape in labriform locomotion (Blake, 1981; Walker and Westneat, 2002). A highly deformable pectoral fin of a bluegill sunfish is superior to a rigid flapping foil in thrust production (Dong et al., 2010); the kinematics of the pectoral fin is very complex and cannot be easily ascribed to a drag- or lift-based mechanism. The animals using drag-based propulsion mode can be found in broad *Re* regimes. The rowing motion of the propulsor is prevalent at *Re*<~15, which implies that the relative magnitude of inertial force and viscous force of surrounding fluid influences the efficiency of drag-based propulsion (Walker, 2002). The interaction between a propulsor and a body is also one of the factors that affect thrust production. The flow structures and forces generated by the propulsor in the absence of the body are different from those of the propulsor closely approaching the body. An animal in drag-based mode may augment thrust by closing its propulsor against its body and squeezing fluid in the backward direction (Blake, 1979; Daniel and Meyhofer, 1989).

In this study, we analyzed the vortex formation process and its relationship with thrust generation using a simple mechanical model mimicking the power stroke of drag-based propulsion. For the mechanical model, we did not consider propulsor–body interaction and used the propulsor alone. First, we investigated the effect of shape and passive deformation of the model on the vortex formation process and propulsive performance. We also studied how flow structure during the power stroke can be different between two different *Re* regimes of $O(10^2)$ and $O(10^4)$. In addition, we explored whether there is an optimal stroke angle for efficient thrust generation and identified important flow phenomena that affect the relationship between stroke angle and thrust performance. In order to map the three-dimensional (3-D) flow field around the model, defocusing digital particle image velocimetry (DDPIV) was implemented (Willert and Gharib, 1992; Pereira and Gharib, 2002; Pereira et al., 2006; Lai et al., 2008).

MATERIALS AND METHODS

Models and kinematic conditions

A plate used as a propulsor was attached to a micro-stepping stepper motor (NEMA 14 and IM483, Schneider Electric Motion, Marlborough, CT, USA). Transparent glass plates with a thickness (h) of 1.15 mm and a density (ρ_m) of 2.56 g cm^{-3} were used as rigid flappers. For the animals in the drag-based mode, the shapes of the propulsors are diverse. In this study, three simple shapes (rectangle, triangle and delta) were considered (supplementary material Fig. S1). All plates had the same area of 6400 mm^2, but the ratio of the plate width of the base to the width of the tip was different. The delta-shaped plate was chosen to represent a propulsor such as a duck's foot, which has a much larger area near the tip than near the base. The width of the rectangular plate was 40 mm. The widths of the tip and the base in the triangular plate were 65 and 15 mm, respectively. The end part of the delta-shaped plate was the equilateral triangle 111 mm wide near the tip. The width of the region connecting the base and the equilateral triangle was 15 mm. The span length from the base to the tip (s) and the mean width ($\bar{c}$) were 160 and 40 mm, respectively, for all plates. The glass plates were assumed to be rigid. In addition, for flexible plates, transparent polycarbonate plates (Young's modulus E=2.3 GPa, density ρ_m=1.2 g cm^{-3}) with thicknesses of 1.52, 1.02 and 0.76 mm were used for the rectangular, triangular and delta-shaped plates.

Each plate was immersed in a glass tank (870×430×360 mm^3) and rotated by the stepper motor (Fig. 2). Two angular velocity programs, trapezoidal and sinusoidal, were used for rotation of the stepper motor (supplementary material Fig. S2). The stroke time (T) was 2.4 s, and the stroke angle (ϕ) was 106 deg for both angular velocity programs. After 2.4 s, the plate stayed at the final position of the power stroke. For all simulations, only one power stroke was simulated. In the trapezoidal velocity program, the

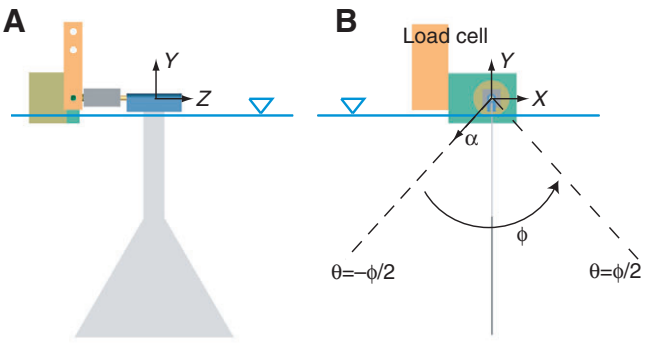

Fig. 2. Schematic of the model. The plate rotates for a stroke angle ϕ with respect to the z-axis in (A) back view and (B) side view (camera view). The rotating axis of the motor is 10 mm above the free surface.

motor accelerated for 0.125 s, maintained a constant angular velocity for 2.15 s and decelerated its rotation for the last 0.125 s. To study flow fields of two different *Re*, water (υ=1 mm^2 s^{-1}, ρ_f=1.00 g cm^{-3}) for high *Re* and mineral oil (Chevron Superla white oil, υ=140 mm^2 s^{-1}, ρ_f=0.84 g cm^{-3}) for low *Re* were used as working fluids inside the tank. The *Re* ($Re = Us/\upsilon$) values were 19,720 and 140 for the high and low *Re* cases, respectively. Span length (s) was used as a characteristic length for *Re* because our main interest was the tip vortex structure at the tip edge of the plate. The characteristic velocity U for *Re* is $s\Omega$, where Ω is the mean angular velocity of the motor during a stroke. In the rigid plate case, U is the same as the mean tip velocity of the plate. In the following sections, the *Re* number of the model is 19,720 unless stated otherwise.

DDPIV and force measurement

DDPIV was conducted to map the 3-D flow generated by a rotating plate. Here, we briefly explain the important processing steps. The DDPIV camera was placed in front of the tank; the distance between the camera and the tank was adjusted to place the camera probe volume in the middle of the tank. The tank was seeded with silver-coated ceramic spheres with a mean diameter of 100 μm (Conduct-o-fil, Potters Industries Inc., Malvern, PA, USA). An Nd:YAG laser (200 mJ pulse^{-1}; Gemini PIV, New Wave Research Inc., Fremont, CA, USA) illuminated the ceramic spheres. The time gap between two laser pulses to take a pair of images was 25 ms. The control computer sent trigger pulses to synchronize operation of the DDPIV camera and the laser, and controlled the stepper motor motion.

First, the 3-D coordinates of the particles inside the tank were determined by matching particle images in three images captured by the DDPIV camera. Then, from the position information of the particles, velocity vectors of the particles were calculated using a relaxation method of 3-D particle tracking (Pereira et al., 2006). The camera probe volume was not large enough to include the whole vortex structure. Thus, three replicates of the experiment were performed by translating the initial position of the model 80 cm and 160 cm parallel to the tank wall. Thus, the total fluid volume mapped by three sets of the experiment was 280×160×160 mm^3. We decided to use 3×3×3 mm^3 cubic grids for the flow field. However, the number of cubic grids in the mapped domain was much larger than the number of randomly spaced velocity vectors obtained from one run, approximately 5000. This number of velocity vectors was obtained from a particle seeding density of approximately 5–10 particles cm^{-3} inside the tank. One of the problems of too dense particle seeding is 3-D ghost particles created artificially by the mismatch of particle images in the three camera sensors (Graff and Gharib, 2008). As the concentration of particles becomes larger, more ghost particles are produced, which may decrease the accuracy of velocity vectors. For this reason, we used a small number of particles and repeated the experiment 25 times under the same conditions with an interval of 90 s in order to increase the number of randomly spaced velocity vectors in a fluid domain. This interval was enough to settle the flow generated by the previous run. For each time step, the randomly spaced velocity vectors obtained from 25 runs were collected. The collected velocity vectors were interpolated into grids of size 3×3×3 mm^3 to produce one velocity field. On each grid point, the velocity vector was obtained from the nearby randomly spaced velocity vectors within 6 mm. In this sense, the velocity field we presented was phase averaged with 25 runs. The vorticity field was derived by a central difference scheme from the velocity field data. The time step between frames was 0.2 s.

For thrust force measurement, a load cell (miniature beam type, Interface Inc., Scottsdale, AZ, USA) was attached to the top of the motor (Fig. 2). The load cell measured the force acting on the plate in the x-direction. Through a signal conditioner (SGA, Interface Inc.), the signal was amplified and filtered with a built-in second-order low-pass filter with a cut-off frequency of 5 Hz. The 5 Hz cut-off frequency of the filter could capture an initial sharp peak at the start of a power stroke. The force was measured three times under the same conditions. The error of the force for the three runs was within 2% of the averaged force value. This error was so small that we present the force measurement result of one run. The thrust coefficient (C_T) and the non-dimensional impulse (I_x) were obtained from the filtered signal:

$$C_T(t_d) = -F_x(t_d) / \frac{1}{2}\rho_f U^2 \hat{r}_2^2 A \quad (4)$$

and

$$I_x(t_d) = \int_0^{t_d} C_T(\tau)\,d\tau / T\ , \quad (5)$$

where U is $s\Omega$, A is the area of the plate, τ is the integral variable for time, T is the total stroke time of the plate and $\hat{r}_2^2$ is the non-dimensional second moment of plate area with respect to the rotating axis. The non-dimensional total impulse (I_∞) is the impulse as t_d goes to ∞.

Variables such as time, velocity, vorticity and circulation were non-dimensionalized with the total stroke time T, the span length s and the velocity U, which is the mean tip velocity in the rigid plate case, as follows: $t=t_d/T$, $\mathbf{u}=\mathbf{u}_d/U$, $\boldsymbol{\omega}=\boldsymbol{\omega}_d s/U$ and $\Gamma=\Gamma_d/Us$, where the subscript 'd' indicates a dimensional variable. MATLAB (The Mathworks Inc., Natick MA, USA) was used to obtain circulation ($\Gamma_d=|\int_A \omega_{zd} dA|$) of the tip vortex at the z=0 plane. A is the whole section of the z=0 plane. The main vorticity component of the tip vortex at the z=0 plane is negative ω_z. In the vorticity plot, some noise vorticity created during the DDPIV process existed in the flow field. Therefore, in evaluating the circulation of the tip vortex, the threshold value of ω_z (ω_z<–0.26) was chosen to include only vorticity inside the tip vortex, but not noise vorticity.

For the flexible plate cases, the flexural stiffness and density of the plate are important parameters in the interaction between a deformable plate and fluid. Two non-dimensional numbers can be induced with these parameters to characterize the fluid–deformable structure interaction problem. Here, non-dimensional flexural stiffness is defined as $EI=(EI)_d/\rho_f U^2 s^3$, where $(EI)_d$ is the dimensional flexural stiffness per unit width. EI is 10.9, 3.2 and 1.4 for the plate thicknesses of 1.52, 1.02 and 0.76 mm, respectively, in water. This non-dimensional parameter indicates the relative magnitude of plate-bending shear force with respect to fluid inertial force. Another non-dimensional parameter, $\rho_m h/\rho_f \bar{c}$, is 0.046, 0.031 and 0.023 for the plate thicknesses of 1.52, 1.02 and 0.76 mm, respectively, in water. This parameter represents the relative magnitude of the inertial force of a spanwise plate section over the acceleration-reaction force of the surrounding fluid at the section.

RESULTS

Vortex structure and spanwise flow distribution

Vortices generated by the power stroke of rectangular, triangular and delta-shaped glass plates are compared in Fig. 3 (supplementary material Movies 1–3) for the trapezoidal angular velocity program (*Re*=19720). Even though the entire plate was immersed into water, except 10 mm near the rotating axis, only the flow field near the tip was mapped from DDPIV. One distinct difference among these three

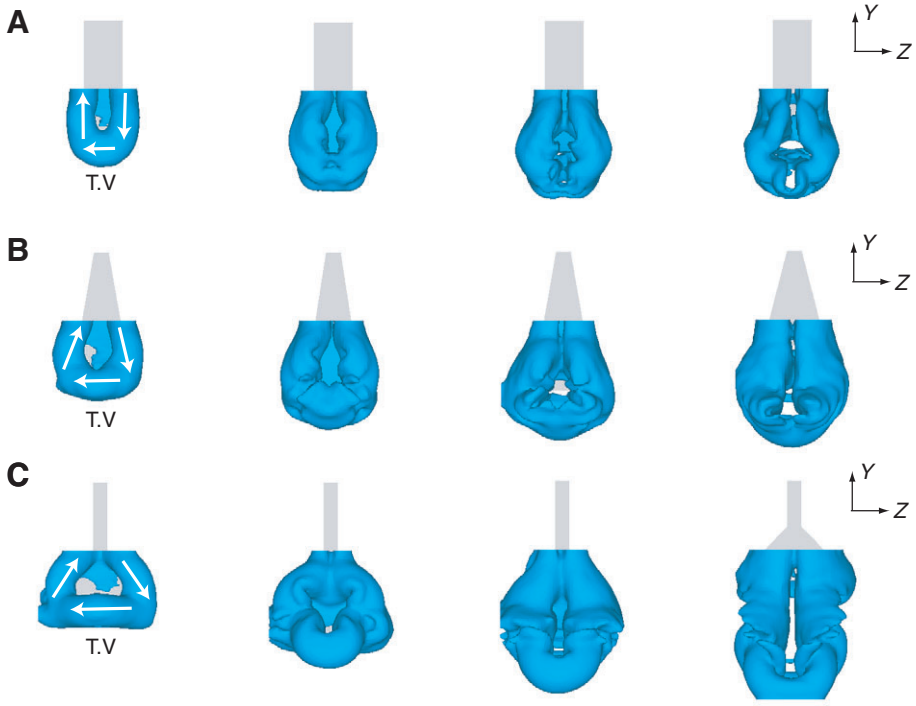

Fig. 3. Vortex structures for three propulsors with different shapes: (A) rectangular, (B) triangular and (C) delta-shaped plates in back view (*Re*=19,720). From left to right, the vortex formation process is shown at four time steps (*t*=0.25, 0.50, 0.75 and 1.00). Iso-surfaces of vorticity magnitude (|ω|=6) are used. The arrows in the first time step show the rotating direction of the vortex. T.V indicates the position of the tip vortex.

cases is the nature of the tip vortex motion. During the stroke, the position of the tip vortex is the lowest along the *y*-direction for the delta-shaped plate and the highest for the rectangular plate. For the delta-shaped plate, soon after the propulsor starts the power stroke, the tip vortex near the tip edge of the plate separates from the tip edge and moves outward from the tip edge. Meanwhile, the tip vortex for the rectangular plate follows the trajectory of the tip edge without significant outward motion.

Spanwise flow distribution behind the rotating propulsor is shown in Fig. 4 at *t*=0.5 when the propulsor surface is parallel to the *y*-axis. Spanwise flow is the flow that has the velocity component in the direction from the base of the plate toward the tip of the plate. Outward spanwise flow is strong and widely distributed for the delta-shaped plate compared with the rectangular plate case. Spanwise flow occurs mainly in the center region between two side-edge vortex cores. The trends of tip vortex motion and spanwise flow distribution mentioned here were also observed with the sinusoidal angular velocity program.

Reynolds number effect

In order to investigate whether the tip vortex motion and spanwise flow distribution are dependent on *Re*, two *Re* cases (*Re*=19,720 and 140) were compared for the rigid delta-shaped plate using the trapezoidal angular velocity program. In the high *Re* case (*Re*=19,720), the effect of fluid viscosity on fluid motion is much smaller than that in the lower *Re* case (*Re*=140). The length scale of vorticity diffusion is approximately proportional to the square root of kinematic viscosity. Because of slow vorticity diffusion, the flow structure behind the plate forms more conspicuous vortex cores in the high *Re* case compared with the low *Re* case (Fig. 5). In the low *Re* case, the tip vortex does not move outward during rotation as much as in the high *Re* case. Moreover, the core of the tip vortex

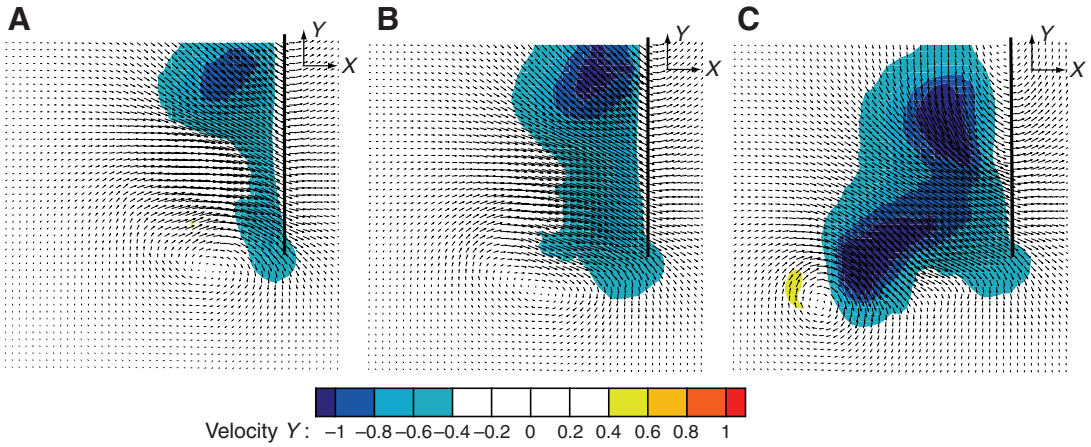

Fig. 4. Spanwise flow distribution for (A) rectangular, (B) triangular and (C) delta-shaped propulsors at *t*=0.50 (side view). The black line is the position of the rotating plate at *t*=0.50. Velocity vectors and velocity *y* contours are plotted on the symmetrical *z*=0 plane.

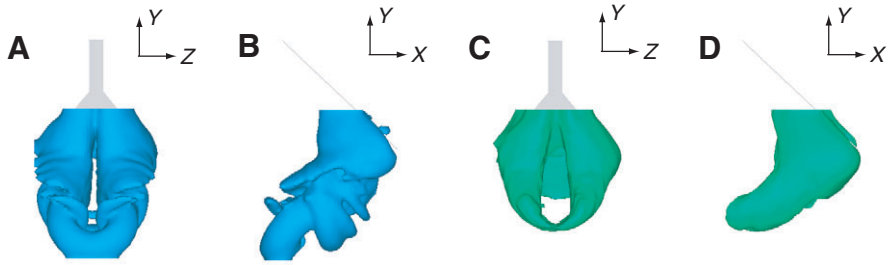

Fig. 5. Comparison of vortex structures between high and low Reynolds numbers at t=0.92 for the rigid delta-shaped plate and trapezoidal angular velocity case (A,B: *Re*=19,720; C,D: *Re*=140). A and C are in back view; B and D are in side view. Iso-surfaces of vorticity magnitude ($|\omega|$=6 for high *Re* and $|\omega|$=4 for low *Re*) are used.

does not show a clear separation from the tip edge. Instead, the core elongates following the tip edge. Spanwise flow of the low *Re* case is not formed as distinctly as that of the high *Re* case. High shear stress due to high fluid viscosity keeps fluid behind the plate from moving toward the tip, the lower pressure region. Most of the flow behind the plate has the velocity component perpendicular to the span of the plate for the low *Re* case. All of these trends are also found for the sinusoidal angular velocity program.

Effect of plate shape and flexibility on thrust performance

Fig. 6 shows thrust coefficients obtained from force transducer measurements for rigid glass plates of the shapes studied here (*Re*=19,720). The three cases do not show a significant difference in thrust coefficients, especially when using the trapezoidal velocity program. In the definition of the thrust coefficient (Eqn 4), the non-dimensional second moments of the plate area $\hat{r}_2^2$ are 0.33 for the rectangular plate, 0.44 for the triangular plate and 0.56 for the delta-shaped plate. Therefore, the delta-shaped plate case generates the largest force during the power stroke (supplementary material Fig. S3).

In order to study the effect of plate flexibility on thrust generation trends, the force was measured with four triangular plates with different flexural stiffnesses (rigid, EI=10.9, 3.2 and 1.4) using the trapezoidal angular velocity program (Fig. 7). If the plate is flexible, the plate is bent backward during impulsive angular acceleration of the plate. The peak of the hydrodynamic force during impulsive acceleration is smoothed out more distinctly as the flexural stiffness is smaller. In spite of bending, the flexible plastic plates can generate more thrust than the rigid glass plate for some time after the angular acceleration phase. In addition to the acceleration phase, the peak in the deceleration phase also tends to be smoothed out for the low flexural stiffness case. Even though the temporal trend of the force acting on the plate is affected by flexural stiffness, total impulse I_∞ is not strongly dependent on it. All four cases have a similar magnitude of total impulse; I_∞ is between 2.10 and 2.15 in the four cases. This does not mean that the propulsor with smaller flexural stiffness can generate a thrust comparable to the above four cases. In our experiment, the plate with EI=0.4 generated a much smaller impulse than the above cases. The plate was bent backward so severely during rotation that the rotational speed of the plate was much smaller than the above cases. In the sinusoidal angular velocity program, the large initial peak of the force is absent even for the rigid plate case, and thus the temporal trend of the thrust is similar for the four flexural stiffness cases.

Optimal stroke angle for thrust

A simple experiment was conducted to determine whether there was an optimal power stroke angle for efficient thrust generation. For rectangular, triangular and delta-shaped rigid plates, the power stroke angle ϕ was varied from 60 to 180 deg in 10 deg increments. The sinusoidal angular velocity program was used in this experiment. The starting and stopping positions of the plate are symmetric with respect to the x=0 plane. These kinematic conditions of a power stroke – sinusoidal angular velocity and symmetry along the x=0 plane – oversimplify the kinematics of propulsors in real animals. In order to avoid the plate moving over the free surface for large stroke angle cases (e.g. 180 deg), in this experiment, the rotating axis of the stepper motor was parallel to the y-axis, and the shaft and the plate were immersed vertically in the tank. The stroke time T of the propulsor is proportional to the stroke angle ϕ; 2.4 s for 180 deg and 1.2 s for 90 deg:

$$\theta = -\frac{\phi}{2}\cos\left(\frac{\pi t_d}{T}\right) \quad (6)$$

and

$$\dot{\theta} = \frac{\phi\pi}{2T}\sin\left(\frac{\pi t_d}{T}\right), \quad (7)$$

where θ is the angle between the plate and the x=0 plane and $\dot{\theta}$ is the angular velocity of the plate (Fig. 2B). For all stroke angles, the mean angular velocity remains constant (θ/T=const), which means that the maximum angular velocity in the middle of a stroke also remains constant. Only one power stroke was considered and, after the power stroke, the plate stayed at the final position of the power stroke without returning to its initial position.

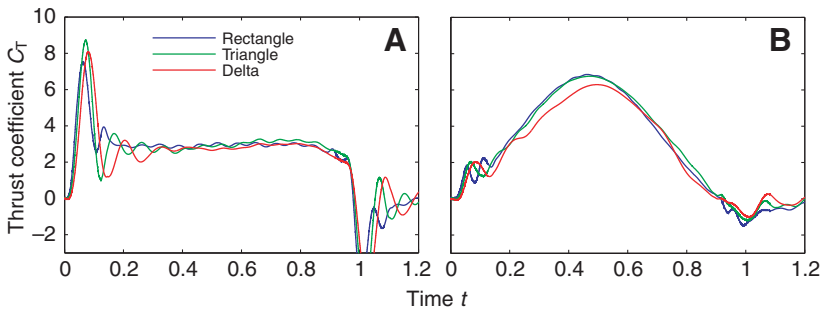

Fig. 6. Shape effect on thrust generation for (A) trapezoidal and (B) sinusoidal angular velocity program cases (*Re*=19,720).

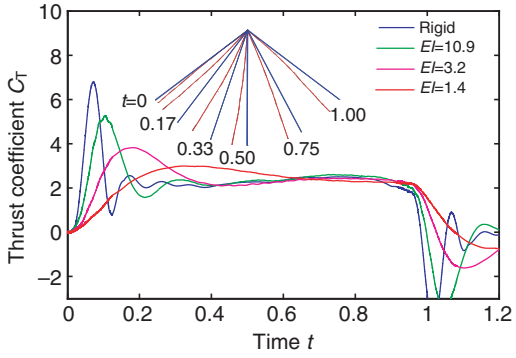

Fig. 7. Flexibility effect on thrust generation for four triangular plates with different flexural stiffnesses in the trapezoidal angular velocity program (*Re*=19,720). Inset: plate shapes of the rigid plate (blue) and the flexible plate (*EI*=1.4; red) during a power stroke in side view.

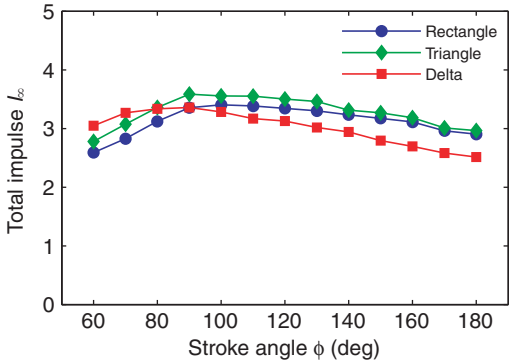

Fig. 8. Dependence of total impulse on stroke angle for the rectangular, triangular and delta-shaped plates.

For the stroke angles between 90 and 180 deg, non-dimensionalized total impulse in the *x*-direction I_∞ has a tendency to increase slightly as the stroke angle decreases (Fig. 8). As the stroke angle decreases further from 90 deg, the total impulse tends to decline steeply except for in the delta-shaped plate case. In all three cases, the stroke angle for the highest total impulse resides between 80 and 100 deg. It is notable that, among the three cases, the delta-shaped plate case has the highest total impulse below ϕ=80 deg whereas it has the lowest total impulse above ϕ=100 deg. For the rectangular and delta-shaped propulsors, the time histories of the impulse I_x for five stroke angle cases are plotted in Fig. 9. In both cases, the lower stroke angle case has the higher peak just before the plate stops. However, for ϕ=60 deg, the impulse decreases significantly near t=1, which results in reduced total impulse. The amount of impulse reduction near the stopping time is much larger for the rectangular plate than the delta-shaped plate.

If the blade element theory is applied to find the best stroke angle for thrust performance in our models, the lower stroke angle should produce the higher non-dimensional total impulse in the *x*-direction. According to the blade element theory, the added-mass effect by acceleration is cancelled by the added-mass effect by deceleration in thrust generation because of the symmetry of the kinematics with respect to the x=0 plane in our models, and there is no force generation after the plate stops rotating. Therefore, we need to consider only quasi-steady force to obtain the total impulse. If C_{qn} is the constant quasi-steady force coefficient acting normally on the plate surface for the section of spanwise width dα, then the total quasi-steady force acting normally on the plate F_{qn} is:

$$F_{qn}(t_d) = \int_0^s \frac{1}{2} C_{qn}\rho_f \left(r\dot{\theta}\right)^2 c(\alpha)\mathrm{d}\alpha = \frac{1}{2} C_{qn}\rho_f \dot{\theta}^2 s^2 \hat{r}_2^2 A \,. \quad (8)$$

Then:

$$I_\infty = \int_0^T F_{qn}(t_d)\cos\theta\,\mathrm{d}t_d / \frac{1}{2}\rho_f U^2 \hat{r}_2^2 AT = C_{qn}\int_0^T \dot{\theta}^2\cos\theta\,\mathrm{d}t_d / \Omega^2 T. \quad (9)$$

With Eqns 6, 7 and 9 and the condition of θ/T=const, it is not difficult to show that I_∞ calculated from the blade element theory increases monotonically as the stroke angle ϕ decreases. This contradicts our result shown in Figs 8 and 9. This argument demonstrates that the application of the blade element theory to the study of drag-based propulsion is questionable.

DISCUSSION

Influence of tip vortex motion and spanwise flow on thrust generation

The outward motion of the tip vortex is enhanced by spanwise flow behind the propulsor. Spanwise flow is mainly distributed in the central region between the cores of side-edge vortices. The spanwise flow induced by the propulsor's motion interacts with the tip vortex and pushes it outward from the tip edge. Once the tip vortex starts to move away from the tip edge, the motion of the tip vortex is less influenced by the motion of the plate. After the separation of the tip vortex core, spanwise flow also interacts with the thin vortex sheet shedding from the tip edge and pushes it outward as well. As the tip edge is wider, the tip vortex tends to move farther away from the tip edge during rotation.

Under the condition that the three propulsors have the same area, it is not difficult to think that the delta-shaped plate may generate the largest thrust because more area is distributed near the tip where the rotational speed is fast. Clearly, the delta-shaped plate generates the largest force during the power stroke. According to Eqns 1–3, the outward motion of the tip vortex in the delta-shaped plate case contributes to the increase in thrust ($-F_x$) by enlarging the inner area enclosed by the vortex structure projected on the *y*–*z* plane. However, one should also notice that, in the delta-shaped plate case, side-edge vortices near the tip tend to move inward, which reduces the inner area of the vortex. These arguments do not mean that the difference in thrust magnitude among the three cases is purely due to the difference in tip vortex motion. To relate thrust and vortex structure, vorticity distribution of the whole vortex structure instead of the tip vortex alone should be taken into consideration.

The role of spanwise flow mentioned in this paper is different from the role of spanwise flow for leading-edge vortex stabilization in hovering insects. In the hovering insect case, it is important to maintain the leading-edge vortex on the wing of hovering insects for high lift generation, and spanwise flow inside the leading-edge vortex has a role in stabilizing the leading-edge vortex by transporting vorticity of the leading-edge vortex toward the tip (Maxworthy, 1979; Ellington et al., 1996). Meanwhile, in our model of drag-based propulsion, spanwise flow is mainly caused by the vortical flows of the side-edge vortices and the bound vortex. The spanwise flow induces the outward motion of the tip vortex rather than maintaining the tip vortex near the tip edge, which is advantageous in thrust performance.

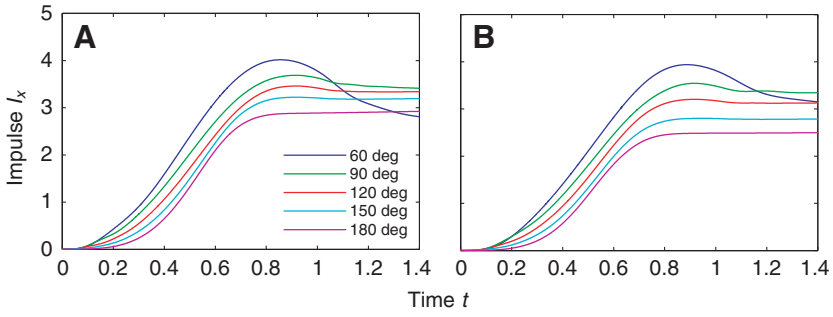

Fig. 9. Impulse for five stroke angles in (A) rectangular and (B) delta-shaped plates.

The tip vortex outward motion depends on *Re*. In the delta-shaped case with *Re*=140, the tip vortex does not move outward as much as in the *Re*=19,720 case, and spanwise flow is not as strong (Fig. 5). A less distinct outward motion of the tip vortex does not mean that thrust is smaller in the low *Re* case than in the high *Re* case. From our experiment, the low *Re* cases were found to generate larger impulses during the stroke (supplementary material Fig. S4). We conjecture that it is because side-edge vortices of the low *Re* case are distributed further outward in the *z*-direction compared with those of the high *Re* case, which contributes to larger thrust.

Change of thrust trend by flexible propulsors

Many studies on the mechanical effect of flexible propulsors have focused on enhanced performance of propulsive force and efficiency by virtue of flexibility (Mountcastle and Daniel, 2009; Young et al., 2009). In our cases of drag-based propulsion, flexible propulsors generate a total impulse similar to that of the rigid propulsor. However, the trend of thrust generation is quite different between rigid and flexible propulsors in the trapezoidal angular velocity program. With smoothed peaks of thrust, the flexible propulsor could generate nearly constant thrust during a power stroke. Some advantages of flexibility can be inferred from this result. The unsteadiness of the thrust is reduced by flexibility in spite of sudden acceleration and deceleration without the sacrifice of total thrust performance, which is good at stabilizing the body during abrupt locomotion. Furthermore, by avoiding large peaks of the force acting on the propulsor, flapping animals will be able to reduce the danger of fracture and fatigue in structures for propulsion.

The shapes of the rigid plate and flexible plate (*EI*=1.4) during rotation are shown in Fig. 7. Because of deflection by gravity, the initial positions of the flexible plate are not the same as that of the rigid plate. During initial acceleration, the rotating motion of the tip part of the flexible plate is delayed because of bending by the hydrodynamic force acting on the plate. The maximum angle difference between the tips of the rigid and flexible plates is 11 deg at *t*=0.25 with respect to the rotating axis. The flexible plate (*EI*=1.4) can generate larger thrust than the rigid plate during the first half of the power stroke (*t*=0.2–0.5 in Fig. 7). For the flexible plate, the bending caused by initial acceleration delays the vortex formation process. However, after the acceleration phase, the vortex starts to develop at a fast pace. Moreover, when the bending of the flexible plate is relaxed due to reduced hydrodynamic force, the tip of the plate moves faster than that of the rigid plate during the remaining first half of the rotation (Fig. 7). The tip motion of the flexible plate is closely related to the trend in the growth of the tip vortex circulation (Fig. 10). The tip vortex circulation of the flexible plate (*EI*=1.4) delays its growth at an initial stage of rotation, but catches up with circulation of the rigid glass plate in the middle of a stroke. For *t*=0.2–0.5, the circulation slope of the flexible plate is larger than that of the rigid plate, which indicates the larger thrust during that time according to Eqns 1–3.

Shedding of stopping vortices

Muskrats and ducklings employing a drag-based propulsion mode use a specific stroke angle for a given body speed (Fish, 1984; Algeldinger and Fish, 1995). Our experiment to find the optimal stroke angle was meant to investigate an important flow phenomenon that can influence a preferred stroke angle. From repeated paddling motions of the propulsor, it has been observed that the ring-like vortex structure is shed into the wake (Algeldinger and Fish, 1995; Drucker and Lauder, 1999). The closed vortex structure in the wake originates from a starting vortex (a tip vortex and side-edge vortices in our case) and a stopping vortex. When the propulsor decelerates its power strokes, the stopping vortex starts to shed from the plate. The shedding process continues even after the propulsor finishes its power stroke. How the stopping vortex is shed depends on the shape and flexibility of the plate and the angular velocity program. For example, the stopping vortex sheds smoothly for the sinusoidal velocity program whereas it sheds abruptly for the trapezoidal velocity program because of its short deceleration time.

The stopping vortex can be shed both from the tip edge and from two side edges of the plate. In all edges, the stopping vortex has vorticity whose sign is opposite to that of the starting vortex. In our experiment, unless the stopping vortex sheds in the direction parallel to the *x*-axis, the shed stopping vortex has a negative effect on thrust ($-F_x$) according to Eqns 1–3. As the stroke angle becomes smaller, this negative effect of the stopping vortex on thrust is amplified because the stopping vortex tends to shed from the tip edge and side edges in the direction perpendicular to the *x*-axis. For this reason, total impulse

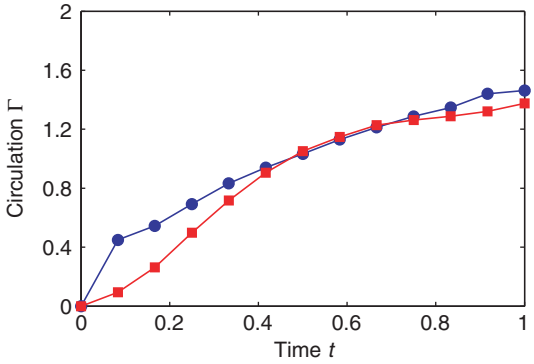

Fig. 10. Growth of the tip vortex circulation for the rigid plate (blue circles) and the flexible plate (*EI*=1.4; red squares). The trapezoidal velocity program was used (*Re*=19,720).

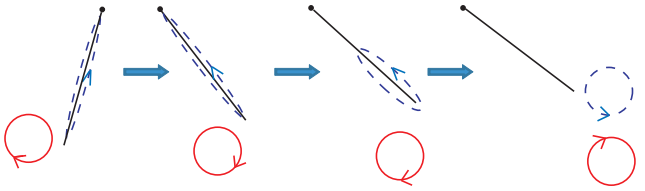

Fig. 11. Formation and shedding of the tip vortex (continuous red lines) and the corresponding bound vortex (dashed blue lines). The shedding bound vortex forms the stopping vortex. Thin blue and red arrows indicate the rotating direction of vorticity (ω_z) on the z=0 plane.

decreases as the stroke angle decreases further from 90 deg in our experiment (Figs 8, 9). For clarity, the formation and shedding of the tip vortex and the corresponding bound vortex are illustrated in Fig. 11. During rotation, the bound vortex is created on the surface of the plate as the counterpart of the starting tip vortex. In deceleration, the bound vortex starts to move toward the tip edge and forms a stopping vortex. This shedding process has a negative effect on thrust generation because it reduces the inner area spanned by the vortex structure.

For the θ=60 deg case of the delta-shaped plate, the decline of the impulse near t=1.0 is small compared with that of the rectangular plate (Fig. 9). One possible reason is the position of the bound vortex on the plate surface. In the delta-shaped plate case, the bound vortex is distributed mainly near the tip during the stroke. Meanwhile, the bound vortex is distributed uniformly from the base to the tip in the rectangular plate case. Thus, during the stopping vortex shedding process, the decrease in the inner area enclosed by the vortex structure ($\dot{S}_x$<0) for the delta-shaped plate may be smaller than that for the rectangular plate. Spanwise flow distribution can also be used to explain this trend. In the small stroke angle case, the flow behind the plate pushes the plate in the positive x-direction when the plate decelerates or stops and causes the negative thrust. For the delta-shaped plate, the flow behind the plate has a stronger spanwise component than the other cases with different plate shapes, which means less impact on the plate. Therefore, the negative effect of the flow behind the plate on thrust is smaller in the delta-shaped plate case than in the other cases.

Concluding remarks

The motion of the mechanical model in our study is simple: a recovery stroke was not considered, and the body (the rotating axis of the model) was fixed. If the forward speed of the body speed increases relative to the stroke speed of the propulsor (advance ratio increases), the advective flow by the body motion will be more influential in the vortex structure near the propulsor, and the unsteady effect on the vortex formation will be reduced. Thus, the arguments of this study may have to be modified in such a case. For example, we conjecture that the distribution of spanwise flow behind the propulsor may become less sensitive to its shape in the large advance ratio regime. Moreover, the propulsor shape changes drastically during the recovery stroke in order to reduce drag, which should be considered to estimate the overall thrust performance. Therefore, a sophisticated model with more realistic kinematic conditions is required in order to investigate thrust performance in forward locomotion. However, the drag-based mode is also employed for maneuvering, such as quick turning. In this case, the effect of advective flow by the forward motion of the body is small, and a single power stroke is important for the generation of impulsive thrust. In spite of our simple model, we expect that the main characteristics of vortex formation and thrust performance that were studied here will help elucidate the fluid mechanics of the drag-based propulsion mode.

LIST OF SYMBOLS

A	area on the z=0 plane
A	plate area
c	width of the plate
$\bar{c}$	mean width of the plate
C_{qn}	quasi-steady force coefficient acting normally on the plate surface
C_T	thrust coefficient
E	Young's modulus
EI	non-dimensional flexural stiffness per unit width
EI_d	dimensional flexural stiffness per unit width
$\mathbf{F}$	hydrodynamic force acting on the object
F_{qn}	total quasi-steady force acting normally on the plate surface
h	thickness of the plate
I_∞	non-dimensional total impulse in the x-direction
I_x	non-dimensional impulse in the x-direction
$\hat{r}_2^2$	non-dimensional second moment of plate area with respect to the rotating axis
s	plate span length
$\mathbf{S}$	vector of the surface spanned by the close vortex loop
S_x	area of $\mathbf{S}$ projected on the y–z plane
t	non-dimensional time
T	stroke time of a plate during the power stroke
t_d	dimensional time
$\mathbf{u}$	non-dimensional velocity
$\mathbf{u}_d$	dimensional velocity
U	characteristic velocity (=$s\Omega$)
V_∞	infinite flow field volume
V_b	body volume
$\mathbf{x}$	non-dimensional coordinate
$\mathbf{x}_d$	dimensional coordinate
α	coordinate along the span of the plate from the base
Γ	non-dimensional circulation of a vortex
Γ_d	dimensional circulation of a vortex
θ	angle between the plate and the x=0 plane
ρ_f	fluid density
ρ_m	plate density
τ	integral variable for time
ϕ	stroke angle of the power stroke
$\boldsymbol{\omega}$	non-dimensional vorticity
$\boldsymbol{\omega}_d$	dimensional vorticity
Ω	mean angular velocity of the motor during rotation

REFERENCES

Algeldinger, T. L. and Fish, F. E. (1995). Hydroplaning by ducklings: overcoming limitations to swimming at the water surface. *J. Exp. Biol.* **198**, 1567-1574.

Blake, R. W. (1979). The mechanics of labriform locomotion. I. Labriform locomotion in the angelfish (*Pterophyllum eimekei*): an analysis of the power stroke. *J. Exp. Biol.* **82**, 255-271.

Blake, R. W. (1980). The mechanics of labriform locomotion. II. An analysis of the recovery stroke and the overall fin-beat cycle propulsive efficiency in the angelfish. *J. Exp. Biol.* **85**, 337-342.

Blake, R. W. (1981). Influence of pectoral fin shape on thrust and drag in labriform locomotion. *J. Zool. Lond.* **194**, 53-66.

Daniel, T. L. and Meyhofer, E. (1989). Size limits in escape locomotion of carridean shrimp. *J. Exp. Biol.* **143**, 245-265.

Dong, H., Bozkurttas, M., Mittal, R., Madden, P. and Lauder, G. V. (2010). Computational modelling and analysis of the hydrodynamics of a highly deformable fish pectoral fin. *J. Fluid Mech.* **645**, 345-373.

Drucker, E. G. and Lauder, G. V. (1999). Locomotor forces on a swimming fish: three-dimensional vortex wake dynamics quantified using digital particle image velocimetry. *J. Exp. Biol.* **202**, 2393-2412.

Ellington, C. P., vandenBerg, C., Willmott, A. P. and Thomas, A. L. R. (1996). Leading-edge vortices in insect flight. *Nature* **384**, 626-630.

Epps, B. P. and Techet, A. (2007). Impulse generated during unsteady maneuvering of swimming fish. *Exp. Fluids* **43**, 691-700.

Fish, F. E. (1984). Mechanics, power output and efficiency of the swimming muskrat (*Ondatra zibethicus*). *J. Exp. Biol.* **110**, 183-201.

Graff, E. C. and Gharib, M. (2008). Performance prediction of point-based three-dimensional volumetric measurement systems. *Meas. Sci. Technol.* **19**, 075403.

Lai, W., Pan, G., Menon, R., Troolin, D., Graff, E. C., Gharib, M. and Pereira, F. (2008). Volumetric three-component velocimetry: a new tool for 3D flow

measurement. In *14th International Symposium on Applications of Laser Techniques to Fluid Mechanics*. Lisbon, Portugal.
Maxworthy, T. (1979). Experiments on the Weis-Fogh mechanism of lift generation by insects in hovering flight. I. Dynamics of the fling. *J. Fluid Mech.* **93**, 47-63.
Mountcastle, A. M. and Daniel, T. L. (2009). Aerodynamic and functional consequences of wing compliance. *Exp. Fluids* **46**, 873-882.
Pereira, F. and Gharib, M. (2002). Defocusing digital particle image velocimetry and the three-dimensional characterization of two-phase flows. *Meas. Sci. Technol.* **13**, 683-694.
Pereira, F., Stuer, H., Graff, E. C. and Gharib, M. (2006). Two-frame 3D particle tracking. *Meas. Sci. Technol.* **17**, 1680-1692.
Vogel, S. (2003). *Comparative Biomechanics: Life's Physical World*. Princeton: Princeton University Press.
Walker, J. A. (2002). Functional morphology and virtual models: physical constraints on the design of oscillating wings, fins, legs, and feet at intermediate Reynolds numbers. *Integr. Comp. Biol.* **42**, 232-242.
Walker, J. A. (2004). Dynamics of pectoral fin rowing in a fish with an extreme rowing stroke: the threespine stickleback (*Gasterosteus aculeatus*). *J. Exp. Biol.* **207**, 1925-1939.
Walker, J. A. and Westneat, M. W. (2000). Mechanical performance of aquatic rowing and flying. *Proc. R. Soc. Lond. B* **267**, 1875-1881.
Walker, J. A. and Westneat, M. W. (2002). Performance limits of labriform propulsion and correlates with fin shape and motion. *J. Exp. Biol.* **205**, 177-187.
Willert, C. and Gharib, M. (1992). Three-dimensional particle imaging with a single camera. *Exp. Fluids* **12**, 353-358.
Wu, J. C. (1981). Theory for aerodynamic force and moment in viscous flows. *AIAA J.* **19**, 432-441.
Wu, J. Z., Ma, H. Y. and Zhou, M. D. (2006). *Vorticity and Vortex Dynamics*. Berlin: Springer.
Young, J., Walker, S. M., Bomphrey, R. J., Taylor, G. K. and Thomas, A. L. R. (2009). Details of insect wing design and deformation enhance aerodynamic function and flight efficiency. *Science* **325**, 1549-1552.